metals

MDPI

Article

Comparative Study of Prior Particle Boundaries and Their Influence on Grain Growth during Solution Treatment in a Novel Nickel-Based Powder Metallurgy Superalloy with/without Hot Extrusion

Yancheng Jin [1], Shiyao Chen [1,*], Xiaoke Wu [1], Jianzheng Guo [1,2] and Lijun Zhang [1,3,*]

[1] State Key Laboratory of Powder Metallurgy, Central South University, Changsha 410083, China
[2] Shenzhen Wedge Central South Research Institute Co., Ltd., Shenzhen 518000, China
[3] Shenzhen Research Institute, Central South University, Shenzhen 518057, China
* Correspondence: chenshiyao@csu.edu.cn (S.C.); lijun.zhang@csu.edu.cn (L.Z.); Tel.: +86-731-8883-6812 (L.Z.); Fax: +86-731-8871-0855 (L.Z.)

Abstract: The prior particle boundaries (PPBs), as one of the typical defects in the nickel-based powder metallurgy superalloy, largely affect the microstructure and thus properties/performance of alloys. However, the effect of PPBs on the microstructure evolution in nickel-based powder metallurgy superalloy during heat treatment is still unclear. In this paper, a comparative study of PPBs and their influence on grain growth during solution treatment in a novel nickel-based powder metallurgy superalloy FGH4113A (i.e., WZ-A3 from Shenzhen Wedge, China) with/without hot extrusion (HEX) was conducted. Firstly, through a combination of scanning electron microscope (SEM), electron probe microanalyzer (EPMA) and transmission electron microscope (TEM) techniques, PPBs in FGH4113A alloys were characterized to be Al_2O_3, carbides (TiC, M_6C, $M_{23}C_6$) and large-size γ' particles. After HEX, the oxides broke, carbides deformed, and γ' phase redistributed. After solution treatment at 950 °C, the TiC decomposed to M_6C and $M_{23}C_6$, while no such decomposition occurred in FGH4113A alloys after solution treated at 1050 °C and 1150 °C. Secondly, the evolution of grain size in FGH4113A alloys was analyzed using the electron backscattered diffraction (EBSD) technique. At 950 °C, the decomposition of carbide TiC resulted in the increase of PPBs and the enhancement of their pinning effect on grain boundaries, thus inhibiting grain growth. At 1050 °C, the nucleation rate due to recrystallization is comparable to the grain growth rate, leading to the stable distribution of grain size. While at 1150 °C, the higher temperature can induce a higher content of PPBs. However, the driving force for grain growth surpassed the pinning force of PPBs, making the grains quickly coarsen. Finally, it was concluded that the HEX process is an effective method to modify the microstructure of powder metallurgy superalloy after HIP that can heavily refine the grains in the powder metallurgy superalloys. Furthermore, based on the present experiment and analysis, an appropriate solution treatment mechanism (i.e., 1050 °C for 2 h) was proposed for FGH4113A alloys.

Keywords: powder metallurgy superalloy; prior particle boundaries; hot extrusion; solution treatment; grain growth

check for updates

Citation: Jin, Y.; Chen, S.; Wu, X.; Guo, J.; Zhang, L. Comparative Study of Prior Particle Boundaries and Their Influence on Grain Growth during Solution Treatment in a Novel Nickel-Based Powder Metallurgy Superalloy with/without Hot Extrusion. *Metals* **2023**, *13*, 17. https://doi.org/10.3390/met13010017

Academic Editor: Andrey Belyakov

Received: 23 November 2022
Revised: 15 December 2022
Accepted: 17 December 2022
Published: 22 December 2022

Copyright: © 2022 by the authors. Licensee MDPI, Basel, Switzerland. This article is an open access article distributed under the terms and conditions of the Creative Commons Attribution (CC BY) license (https://creativecommons.org/licenses/by/4.0/).

1. Introduction

Owing to their excellent high-temperature mechanical properties, oxidation resistance, and long fatigue life, nickel-based superalloys are extensively used in the aeroengines [1–5]. As one of the most important parts in the aeroengine, the turbine disc is usually fabricated by powder metallurgy technique [6], which can produce samples/parts with more homogeneous microstructure, less segregation, higher yield strength, and longer fatigue life than the traditional casting-forging technique [7–9]. The generally adopted preparation

process of powder metallurgy superalloys includes vacuum induction melting, preparation of pre-alloyed powder, powder pretreatment, hot isostatic pressing (HIP), hot working, nondestructive testing, and heat treatment [10–13]. However, the powder metallurgy technique brings some defects such as inclusion, thermal-induced pore (TIP), and prior particle boundaries (PPBs) into the nickel-based superalloys [14–16], especially during the powder preparation and HIP processes. The first two types of defects can be eliminated by post-processing methods according to previous studies [17,18]. As for the PPBs, it is hard to completely remove them from alloys once formed [19]. In general, the PPBs consist of oxides, carbides, and large γ' particles [20,21]. PPBs can impede the diffusion and metallurgical bonding process among powder particles and be prone to crack initiation and thus deteriorate the mechanical properties of the alloys [22,23]. More importantly, PPBs may also restrain the grain growth during heat treatment, leading to a decrease in the high-temperature creep-resistant performance of the alloys [24].

Up to now, many research groups have devoted their efforts to eliminating the PPBs in powder metallurgy superalloys by adjusting the alloy composition [25–27], pre-treating the powder [28], or optimizing the preparation processes [29]. Moreover, after the PPBs form, some further treatments, like the high-temperature solution treatment [30] and the hot extrusion (HEX) process [31], have also been utilized. Particularly, the HEX process after HIP is commonly used to reduce the impact of PPBs. For instance, Higashi et al. [32] reported that the HEX process can be used to refine the microstructure and disperse the PPBs. Tan et al. [33] found that the PPBs can be broken after the HEX process. Moreover, previous studies have proved that the HEX process can provide an effective way to adjust and optimize the microstructure of powder metallurgy superalloys [31–33]. The HEX process was also applied in Fe-Ni-Zr alloys by the group at the United States Army Research Laboratory (ARL) [34–36], in which a nano-dispersion of Zr-oxides was found in the matrix of alloys after equal channel angular extrusion (ECAE). Furthermore, Song et al. [37] investigated the effect of γ' particles and carbides on Zener, limiting grain size in nickel-based powder metallurgy superalloy, however, the effect of PPBs on the grain size evolution process during solution treatment was not studied, and there is little such relevant study in the literature. In order to perform a microstructural control in powder metallurgy superalloys with PPBs, a detailed study on the evolution of PPBs in the powder metallurgy superalloys with/without hot extrusion and their effect on grain growth during the subsequent solid solution treatment is highly needed, but such study is still missing in the literature.

Consequently, a comparative study of PPBs and their influence on grain growth during solution treatment in a novel nickel-based powder metallurgy superalloy with/without hot extrusion is to be conducted in this paper. Here, the FGH4113A (i.e., WZ-A3) alloy, as a novel powder metallurgy superalloy developed by Shenzhen Wedge Central South Research Institute Co., Ltd., China [38], is chosen as the target. The FGH4113A alloy samples after HIP and HIP + HEX serve as the initial state and are then subject to a series of solution treatments. Afterward, a combination of experimental techniques, including scanning electron microscope (SEM), electron probe microanalyzer (EPMA), transmission electron microscope (TEM), and electron backscattered diffraction (EBSD) techniques will be employed to perform the detailed microstructural characterization of the FGH4113A alloys in different states, from which the conclusions can be finally drawn.

2. Materials and Methods

The chemical composition of the FGH4113A alloy determined using the inductively coupled plasma (ICP) technique is listed in Table 1. The vacuum induction melting, and Argon gas atomization techniques were used for the preparation of pre-alloyed powder. The powders within 53 μm in diameter were screened out and encapsulated in the mold after vacuum degassing. Then, the densification process was implemented for powder particles through hot isostatic pressing (HIP) for 4 h at 1150 °C under the pressure of 150 MPa, followed by furnace cooling to room temperature. After that, some HIP billets were extruded at the extrusion ratio of 4:1~5:1. The extrusion temperature was set to be

1100 °C~1150 °C, and the extrusion speed was 30~50 mm/s. The HIPed and HIP + HEXed alloys were received as the initial state. Finally, the initial alloys with/without the HEX process were cut into small cubes of 5 mm × 5 mm × 5 mm in size, and were solution heat-treated in a high-temperature vacuum tube furnace (GSL1700X, Hefei Kejing Materials Technology Co., Ltd., Hefei, China). The solution treatment conditions are given in Table 2.

Table 1. Chemical composition of FGH4113A alloy.

Element	C	Co	Cr	Mo	W	Al	Ti	Nb	Ta	Hf	Ni
wt.%	0.026	19.05	13.03	4.03	3.98	3.03	3.66	1.22	0.94	0.19	Bal.

Table 2. Solution treatment mechanisms for FGH4113A alloy.

Solution Temperature/°C	950	1050	1150
Solution time/h	4	2	0.5
	8	4	1
	12	6	2

The microstructures of FGH4113A alloys with/without HEX process were characterized using SEM (QuantaTM 250 FEG, FEI, Hillsboro, OR, USA) and TEM (Talos F200X G2, Thermo Fisher Scientific Inc., Waltham, MA, USA). The chemical compositions of the PPBs were analyzed using EPMA (JXA-8530F, JEOL, Tokyo, Japan). The grain size and crystal orientation information were obtained by EBSD (NordlysMax3, OXFORD Instruments, Oxford, UK). As for alloys with HEX, the observed plane is normal to the extrusion direction. The specimens for SEM were ground, polished and etched with 5 g $CuCl_2$ + 100 mL HCl + 100 mL ethanol for 10 s. The specimens for TEM were prepared by Focused Ion Beam (FIB, Helios 5 CX, Thermo Fisher Scientific Inc., Waltham, MA, USA) and the diffraction spot images were processed by Digital Micrograph software (3.11.2, Gatan DigitalMicrograph, USA). The specimens for EBSD were vibration polished for 4 h to relieve the stress in the alloys and the data were processed by Channel5 software (5.0.9.1, HKL CHANNEL5, UK).

3. Results and Discussion

3.1. Characterization and Distribution of PPBs in FGH4113A Alloys with/without HEX

Figure 1 shows a comparison of the PPBs microstructure of FGH4113A alloys in different states with/without HEX, together with the measured chemical compositions of different PPBs in Figure 1b. For FGH4113A alloys without HEX, two types of PPBs were found before and after solution treatment, as clearly shown in Figure 1a,b,d,e. The white particles (shown in Figure 1a,d) are typically small in size (lower than 5 μm in general), while the black particles (shown in Figure 1b,e) are relatively larger (ca. 5~10 μm in diameter). Moreover, it is noteworthy that the black particles are surrounded by white particles, as indicated in Figure 1b,e. Based on the chemical compositions of different PPBs measured by EPMA technique in Figure 1b, the black particles were roughly identified as aluminum-rich oxides, while the white particles were carbides with strong carbide-forming elements such as Zr, Hf, Ti, Ta, and so on. After HEX, the aluminum oxide particles in FGH4113A alloys were broken into finer ones, and thus, one cannot easily observe the black aluminum oxides in Figure 1c,f. By contrast, the white carbides can be clearly observed in Figure 1c,f. Furthermore, after solution treatment, a network of white carbides along the grain boundary gradually forms in FGH4113A alloy as shown in Figure 1d. The EPMA maps for different elements of the selected area in FGH4113A alloys with HEX after solution treatment at 950 °C for 12 h are given in Figure 2. Obviously, the large-size γ' particles, rich in Al, Ni, and Ti along the grain boundaries, also representing one type of PPBs, can be observed.

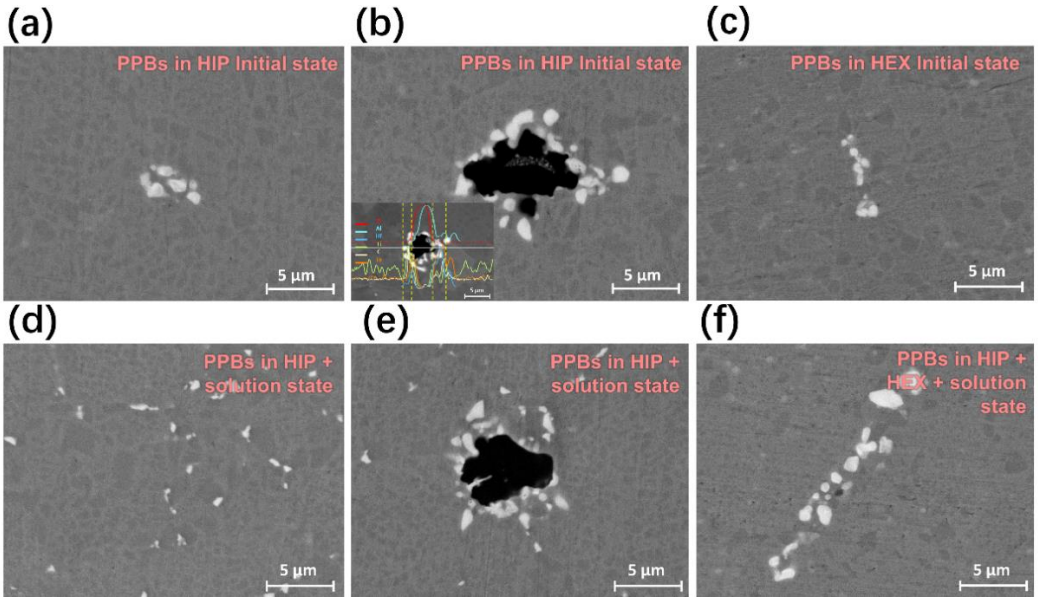


Figure 1. Morphology of PPBs in FGH4113A alloy of (**a**) initial state without HEX, (**b**) initial state without HEX and the element distribution, (**c**) initial state with HEX, (**d**) solution-treated state without HEX (950 °C for 12 h), (**e**) solution-treated state without HEX (950 °C for 12 h), and (**f**) solution-treated state with HEX (1150 °C for 2 h).

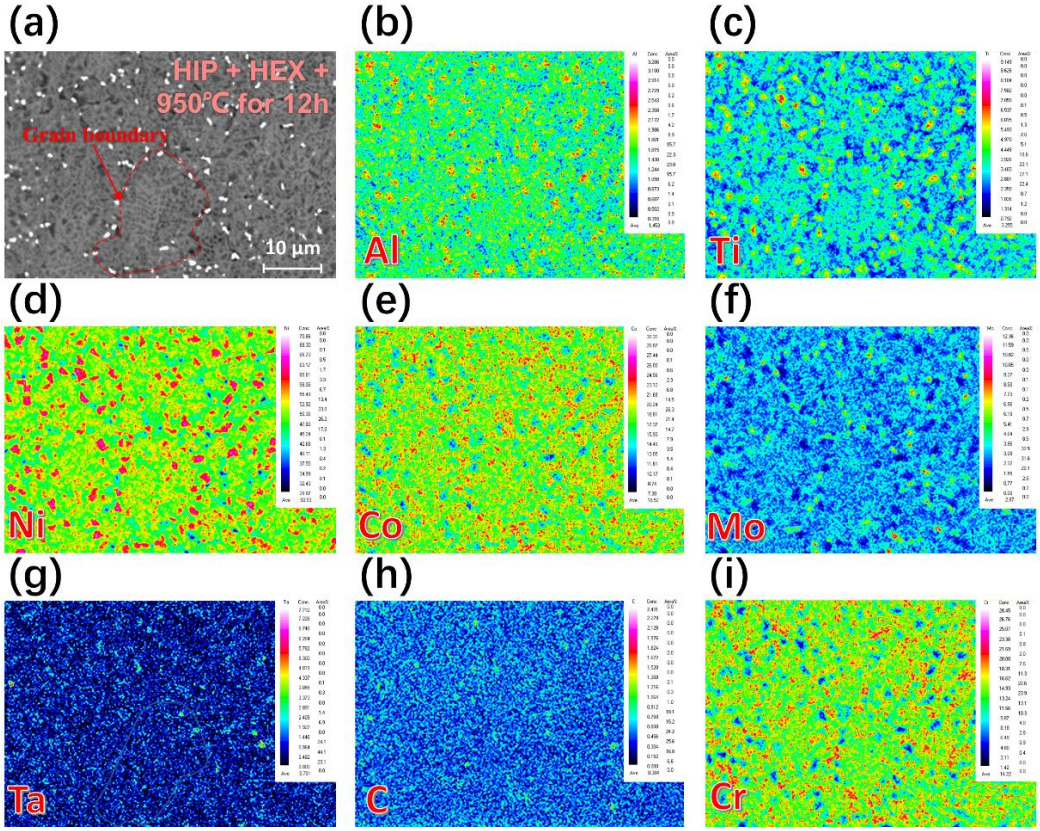


Figure 2. Elements mapping in alloy after HIP + HEX + solution treatment at 950 °C for 12 h: (**a**) BSE image of alloy, and (**b**–**i**) element distribution map of Al, Ti, Ni, Co, Mo, Ta, C, Cr.

Figure 3 presents the bright-field TEM images of FGH4113A alloys in different states with/without HEX. According to the electron diffraction pattern in Figure 3a, the aluminum oxides were confirmed in FGH4113A alloy after HIP. For the carbides, three types, i.e., TiC,

M_6C, and $M_{23}C_6$, were observed on the basis of electron diffraction patterns of FGH4113A alloys in different states. In initial FGH4113A alloys (see Figure 3a,b), only TiC can be seen. While in FGH4113A alloys after solution treated at 950 °C (see Figure 3c,d), only M_6C and $M_{23}C_6$ were observed. This fact indicates that TiC decomposed into M_6C and/or $M_{23}C_6$ at 950 °C. According to the experimental observation of Liu et al. [39] and Matysiak et al. [40], the MC carbides can transform into M_6C (at 815~980 °C) and/or $M_{23}C_6$ (at 760~980 °C) through the following equation:

$$MC + \gamma \rightarrow M_{23}C_6 \text{ and/or } M_6C + \gamma' \quad (1)$$

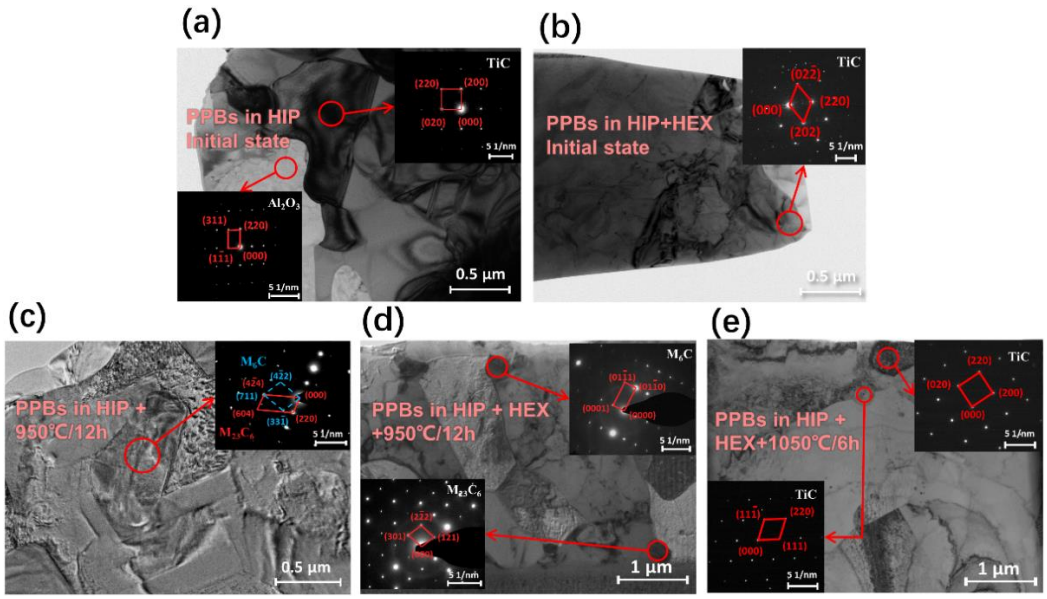


Figure 3. Microstructure and SAED images of precipitates in FGH4113A alloy of (**a**) initial alloy without HEX, (**b**) initial alloy with HEX, (**c**) solution-treated state without HEX (950 °C for 12 h), (**d**) solution-treated state with HEX (950 °C for 12 h), and (**e**) solution-treated state with HEX (1050 °C for 6 h).

Furthermore, in alloys after solution treated at 1050 °C, the carbides still exist in the form of TiC (see Figure 3e). Therefore, at 1050 °C and 1150 °C, the existing TiC did not decompose, and only grew through the diffusion process of carbon and carbide-forming elements.

Figure 4 displays the microstructure of the initial FGH4113A alloys with/without HEX on a relatively large-length scale. The microstructure of FGH4113A alloys with/without the HEX process after solution treatment are shown in Figures 5 and 6, respectively. A rough comparison between Figure 4 and Figures 5 and 6 indicates that more PPBs (especially carbides) appeared in alloys after solution treatment. Moreover, the amount of carbides in FGH4113A alloys depends strongly on the solution mechanisms: (i) For each temperature, the longer the solution time is, the more carbides appear; (ii) For the same solution time, the number of carbides in alloys solution treated at 950 °C is largest, followed by 1150 °C, and then 1050 °C. Based on the TEM analysis, the decomposition of TiC at 950 °C caused more PPBs to appear, while at 1050 °C and 1150 °C, the diffusion-controlled growth process of TiC generates fewer PPBs. On account of the higher temperature, the diffusion process was accelerated and more carbides formed after solution treatment at 1150 °C than that at 1050 °C.

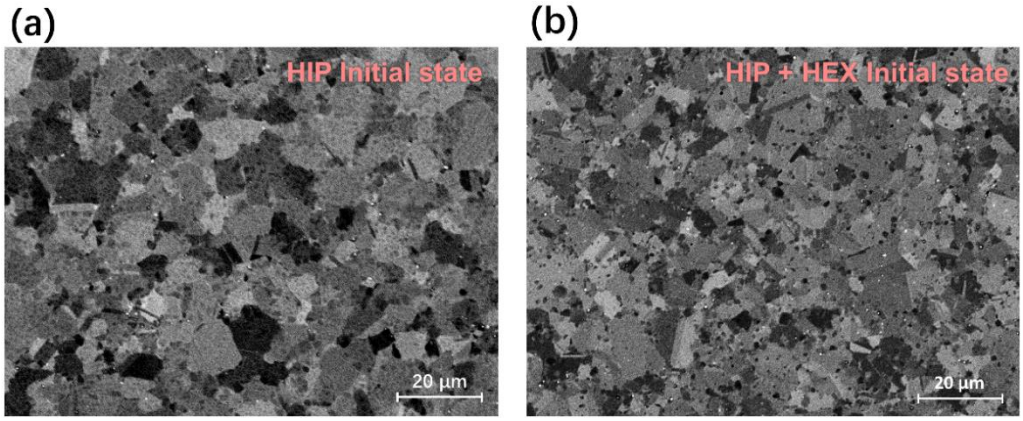


Figure 4. Microstructure of initial FGH4113A alloys (**a**) without HEX, and (**b**) with HEX.

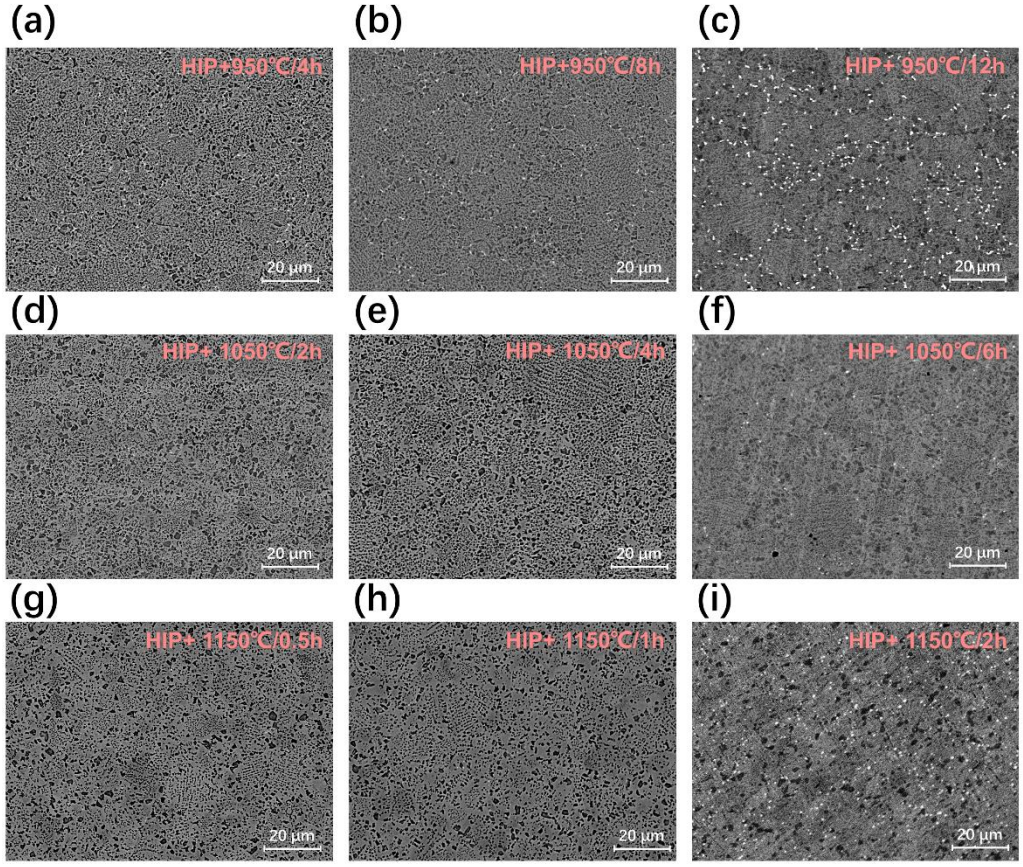


Figure 5. Microstructure of FGH4113A alloys without HEX after solution treatment state: (**a**) 950 °C/4 h, (**b**) 950 °C/8 h, (**c**) 950 °C/12 h, (**d**) 1050 °C/2 h, (**e**) 1050 °C/4 h, (**f**) 1050 °C/6 h, (**g**) 1150 °C/0.5 h, (**h**) 1150 °C/1 h, and (**i**) 1150 °C/2 h.

As observed in Figure 4, the contrast between different grains is noticeable. However, such contrast in the microstructure of Figures 5 and 6 is not obvious. Instead, the large γ' particles corresponding to the etch pits of the microstructure can be clearly seen located along the grain boundaries in, i.e., Figure 6d,e. A detailed comparison between Figures 5 and 6 suggests that the γ' particles distribute homogenously inside grains and along the grain boundaries in FGH4113A alloys without HEX. While in FGH4113A alloys with HEX, the γ' particles inside grains dramatically decrease and are mainly located along the grain boundaries. Such redistribution of γ' particles in alloys with HEX may be caused

by the dynamic recrystallization (DRX) in the HEX process [41,42]. During DRX, the γ' particles tend to precipitate along the grain boundaries [43].

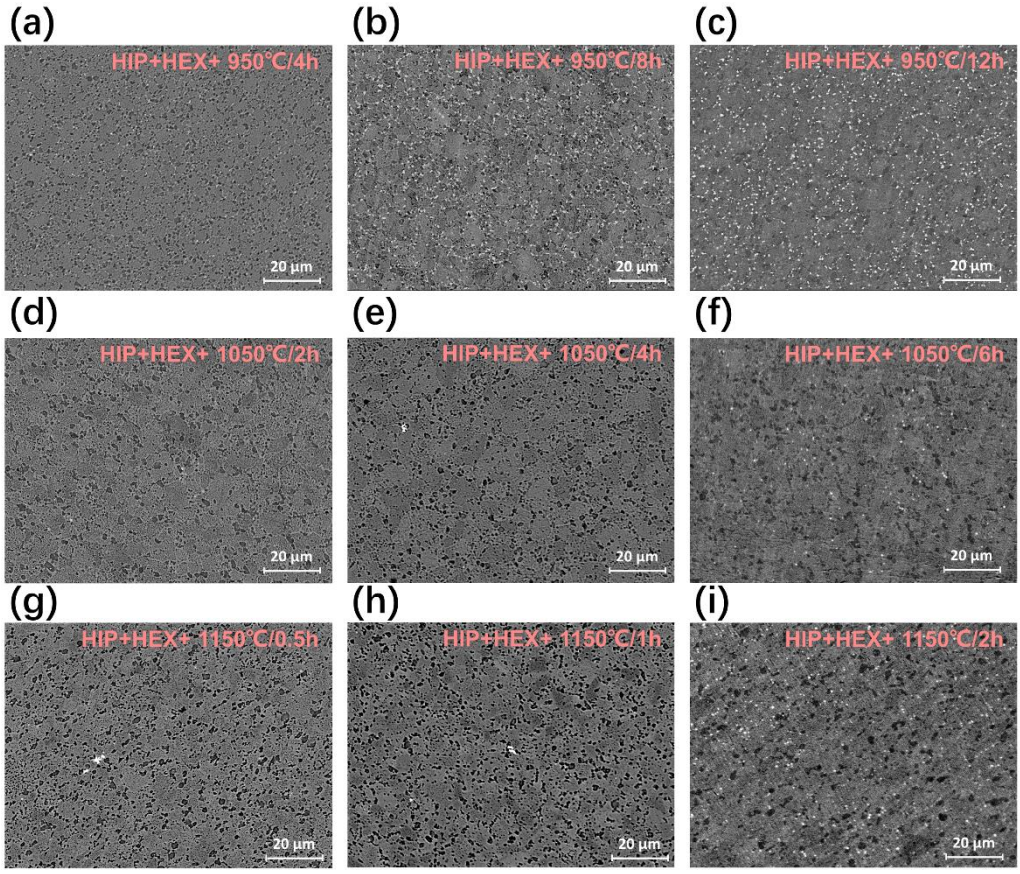


Figure 6. Microstructure of FGH4113A alloys with HEX after solution treatment state: (**a**) 950 °C/4 h, (**b**) 950 °C/8 h, (**c**) 950 °C/12 h, (**d**) 1050 °C/2 h, (**e**) 1050 °C/4 h, (**f**) 1050 °C/6 h, (**g**) 1150 °C/0.5 h, (**h**) 1150 °C/1 h, and (**i**) 1150 °C/2 h.

3.2. Effect of PPBs on γ Grain Growth in Alloys with/without HEX

The FGH4113A alloys with different solution mechanisms with/without HEX were characterized using the EBSD technique, and the resultant inverse pole figure (IPF) coloring maps are given in Figures 7–9. In such IPF maps, different colors represent different crystal orientations. The specific orientation refers to the standard color contrast chart at the left bottom of the figures. The measured average grain sizes for FGH4113A alloys with different solution mechanisms are marked in each figure, and the corresponding grain size distributions are shown in Figure 10. All the statistical results were obtained according to the following assumptions, i.e., (i) that only grains in the neighbor of which orientation difference larger than 10° were treated as separate ones; and (ii) that the grains with the equivalent diameter less than 0.6 μm were disregarded.

According to the IPF maps in Figure 7, the crystal orientations of γ grains in the initial FGH4113A alloys with/without HEX are randomly distributed, inferring that no preferred orientation(s) were caused by HEX process (which can be further confirmed by the pole figure shown in Figure S1). Moreover, the average grain size of the γ matrix in the FGH4113A alloy without HEX is 2.67 μm, while that with HEX is 1.62 μm, indicating that the HEX process can largely decrease the grain size of the γ matrix in FGH4113A alloys. This fact can be also seen in Figure 10, in which the proportion of grains smaller than 2 μm dramatically increases from the FGH4113A alloy without HEX to that with HEX, while that of grains over 4 μm decreases. On one hand, the HEX process can cause grain crushing in FGH4113A alloys, resulting in a significant decrease in grain size. On the

other hand, many DRX grains nucleate and grow in the FGH4113A alloy during HEX, also leading to an increase in the number of small grains. Figure 7c,d are the kernel average misorientation (KAM) maps of the two initial FGH4113A alloys, which are correlated with the level of dislocation density [44]. Based on the KAM map, after HEX, the severe deformation generates a large number of dislocations; a certain amount of strain energy was stored in the alloy.

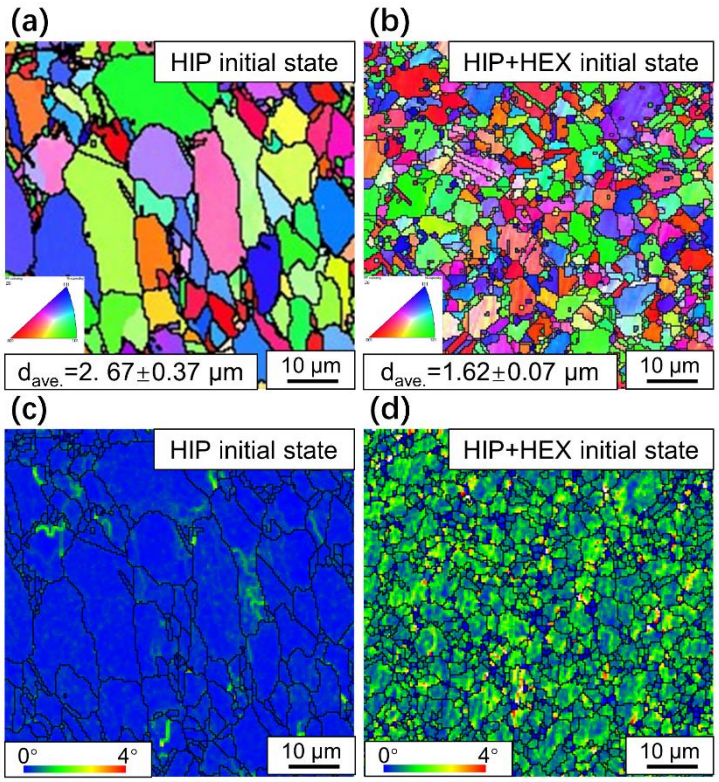


Figure 7. EBSD results of initial FGH4113A alloys (**a**) IPF map without HEX, (**b**) IPF map with HEX, (**c**) KAM map without HEX, and (**d**) KAM map with HEX.

Figures 8 and 9 display the IPF maps of FGH4113A alloys with/without HEX after solution treatment, respectively. From those IPF maps, the following conclusions can be drawn: First, even after solution treatment, the crystal orientations of γ grains are also randomly distributed, and no preferred orientation(s) appears in the alloys (which can be further confirmed by the pole figures shown in Figures S2–S4); Second, based on the IPF maps, the average grain size in FGH4113A alloys with HEX after solution treatment is generally much lower than that without HEX, which is inherently caused by the similar difference in average grain sizes of two initial FGH4113A alloys. Furthermore, comparing alloys with/without HEX, higher dislocation density was caused by HEX, which lead to a higher nucleation rate of recrystallized grains during solution treatment. This will increase the number of small grains and thus deteriorate the high-temperature performance [45], therefore, the subsequent solution treatment is needed to alleviate this effect. Third, the grain growth behavior varies with the solution mechanisms: (i) At 950 °C, the decomposition of TiC caused the increase in the number of PPBs and the enhancement of their pinning effect on grain boundaries. Furthermore, the lower temperature corresponds to the lower mobility of atoms near the grain boundaries, thus leading to the grain boundary migration process slowing down. Based on Figure 10, after being solution treated at 950 °C, grains with a diameter of less than 2 μm slowly decreased in alloys without HEX, leading to the increase in average grain size. In alloys with HEX, due to the higher dislocation density, recrystallization may take place [42]. The nucleation rate of recrystallized grains surpassed the speed of grain growth, resulting the decrease in average grain size after 4 h

of solution treatment (from 1.62 μm to 1.50 μm). The fraction of grains with a diameter less than 2 μm kept stable. (ii) At 1050 °C, the TiC did not decompose and only grew through the diffusion process, resulting in a microstructure with a low content of PPBs. The low content of PPBs at 1050 °C might lower the pinning effect on the grain boundary compared with that at 950 °C. According to Figure 10, the grain size distribution is still very stable during the solution process, which might be attributed to the competition between the nucleation of recrystallized grains and the grain growth behavior during solution treatment. In particular, at 1050 °C, in alloys with HEX, the higher dislocation density accelerates the recrystallization process, and plenty of the newly nucleated recrystallization grains caused the decrease in average grain size (from 2.26 μm to 2.00 μm) with the extension of solution time. (iii) At 1150 °C, TiC did not decompose either, but the diffusion process is faster than that at 1050 °C, thus generating more carbides; Furthermore, the recrystallization starts earlier and the grain boundary migration process is faster than that at 1050 °C. According to the evolution of average grain size at 1150 °C, it can be inferred that after 0.5 h of solution treatment, the nucleation of recrystallization grains predominates in the evolution of grain size distribution, causing the decrease of average grain size in alloys with HEX (1.62 μm to 1.59 μm). As the solution time evolves, the driving force for grain growth surpassed the pinning effect of PPBs on grain boundaries, and the growth of grains predominates in the evolution of grain size distribution, resulting in the increase of average grain size. As can be seen in Figure 10, as the solution time continuously evolves, the grains with diameters less than 2 μm obviously decreased and grains with diameters between 2 and 8 μm increased, which indicates that the increase in average grain size is mainly attributed to the coarsening of small grains.

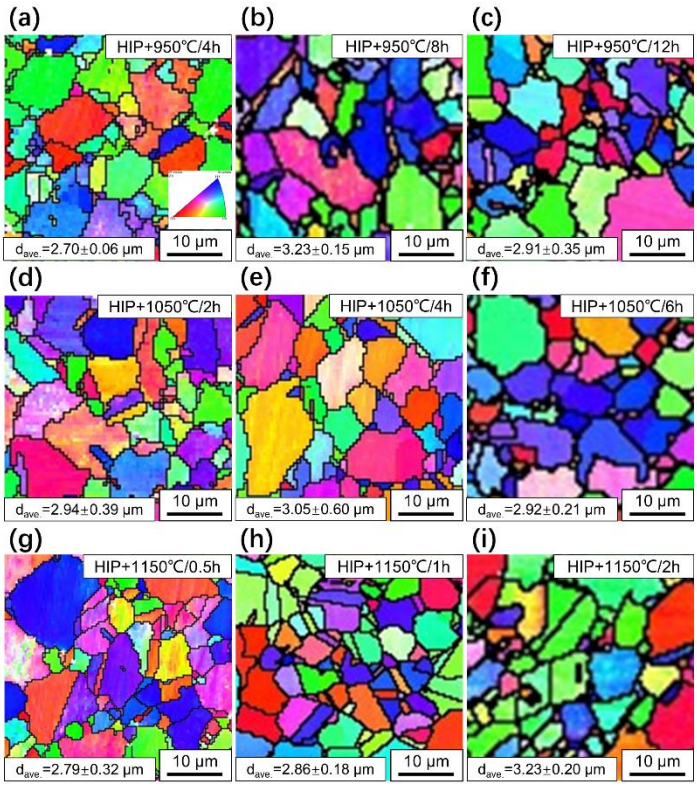


Figure 8. IPF map of FGH4113A alloys without HEX after solution treatment: (**a**) 950 °C/4 h, (**b**) 950 °C/8 h, (**c**) 950 °C/12 h, (**d**) 1050 °C/2 h, (**e**) 1050 °C/4 h, (**f**) 1050 °C/6 h, (**g**) 1150 °C/0.5 h, (**h**) 1150 °C/1 h, and (**i**) 1150 °C/2 h.

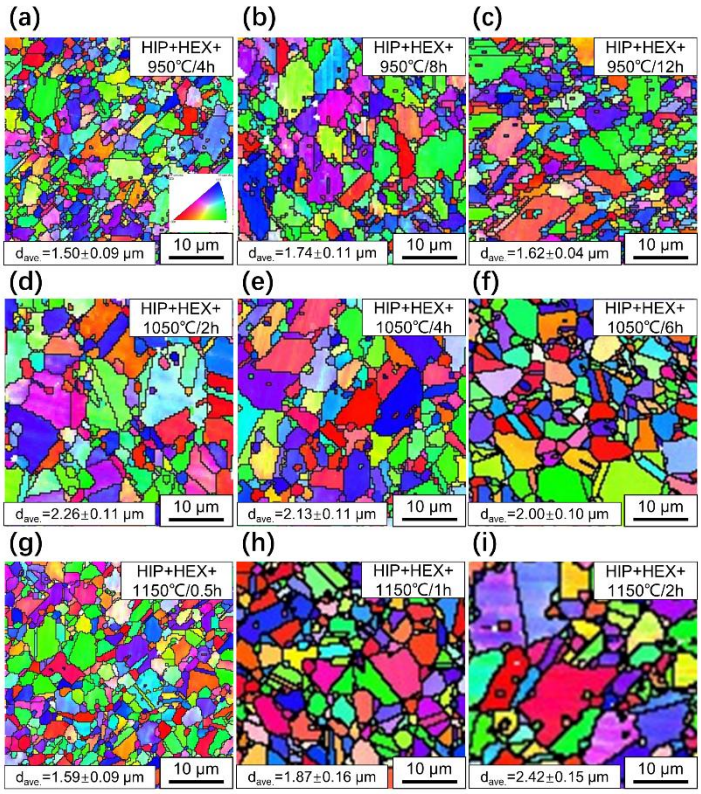


Figure 9. IPF map of FGH4113A alloys with HEX after solution treatment: (**a**) 950 °C/4 h, (**b**) 950 °C/8 h, (**c**) 950 °C/12 h, (**d**) 1050 °C/2 h, (**e**) 1050 °C/4 h, (**f**) 1050 °C/6 h, (**g**) 1150 °C/0.5 h, (**h**) 1150 °C/1 h, and (**i**) 1150 °C/2 h.

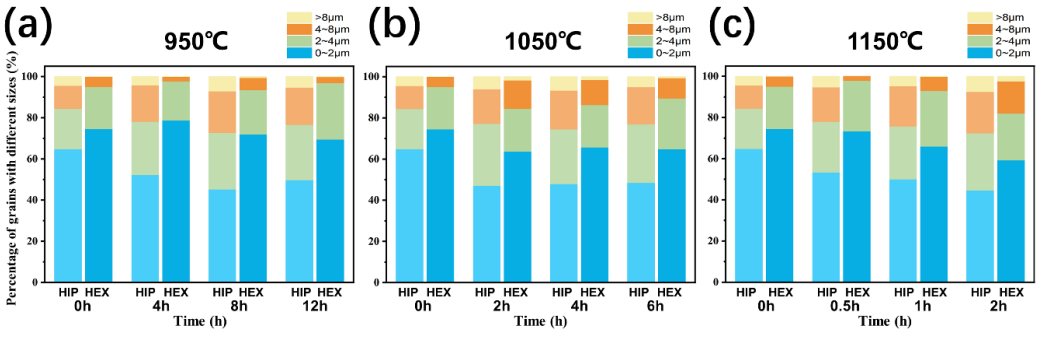


Figure 10. Average grain size distribution of FGH4113A alloys at different solution temperatures: (**a**) 950 °C, (**b**) 1050 °C, (**c**) 1150 °C.

In a short, the content of PPBs generally increased after solution treatment in both alloys with/without HEX, and the grains were strongly pinned at 950 °C but their sizes increased quickly at 1150 °C. At the service temperature of the turbine disk (600~1000 °C), the grain boundary strength may decline [24], and a larger grain size can improve the high-temperature creep resistance. Although the average grain size after solution treated at 1150 °C for 2 h is larger than that at 1050 °C, its high-temperature creep resistance is better and is more suitable for the service condition, however, the higher content of MC-type carbides will deteriorate the creep property of the FGH4113A alloy [46], and the comprehensive mechanical property will decline. Therefore, 1050 °C is a considerable temperature for the solution process of the FGH4113A alloy.

4. Conclusions

- In FGH4113A alloys with different states, PPBs generally consist of aluminum oxides, carbides and large-size γ' particles. Three different types of carbides were observed in total, including TiC, M_6C, and $M_{23}C_6$. Furthermore, the oxides were found to be surrounded by carbides. After HEX, the oxides broke, carbides deformed, and γ' phase redistributed. A network of carbides along the grain boundary gradually appeared with the extension of solution time.
- It was interestingly found that TiC decomposed to M_6C and $M_{23}C_6$ at 950 °C, leading to the increase of PPBs and their pinning effect on grain boundaries, while at 1050 °C and 1150 °C, TiC did not decompose and only coarsened through the diffusion process. In this case, a higher temperature (i.e., 1150 °C) yields a higher content of PPBs than the lower one (i.e., 1050 °C).
- The evolution of grain size in FGH4113A alloys with/without HEX during solution treatment was influenced by solution temperature, solution time, the content of PPBs, and the dislocation density. The HEX process resulted in the higher dislocation density in alloys, leading to a higher nucleation rate during the recrystallization process, and thus caused a higher proportion of small grains and a decrease in average grain size. During the solution treatment at 950 °C, grain boundaries were pinned by the increase of PPBs caused by the decomposition of TiC. While at 1050 °C, the competition between the nucleation of grains in the recrystallization process and the grain growth behavior resulted in a stable distribution of grain size. At 1150 °C, the driving force for grain boundary migration surpassed the pinning force of PPBs, and the grains thus coarsened quickly.
- It can be concluded that HEX is an effective technique for modifying the microstructure of powder metallurgy superalloy. Furthermore, based on a comprehensive comparison of the microstructures in FGH4113A alloys at different solution temperatures, 1050 °C for 2 h was proposed as an ideal solution mechanism for the FGH4113A alloy because of the lowest content of PPBs, appropriate average grain size, and stable grain size distribution.

Supplementary Materials: The following supporting information can be downloaded at: https://www.mdpi.com/article/10.3390/met13010017/s1, Figure S1: Pole figures of the initial FGH4113A alloys with/without HEX; Figure S2: Pole figures of the FGH4113A alloys with/without HEX after solution treated at 950 °C; Figure S3: Pole figures of the FGH4113A alloys with/without HEX after solution treated at 1050 °C; Figure S4: Pole figures of the FGH4113A alloys with/without HEX after solution treated at 1150 °C.

Author Contributions: Data curation, Y.J., S.C. and X.W.; Formal analysis, Y.J.; Funding acquisition, J.G. and L.Z.; Investigation, Y.J., S.C. and X.W.; Methodology, Y.J., S.C., X.W. and L.Z.; Project administration, J.G. and L.Z.; Resources, J.G. and L.Z.; Supervision, L.Z.; Validation, Y.J. and L.Z.; Writing—original draft, Y.J. and L.Z.; Writing—review and editing, Y.J., J.G. and L.Z. All authors have read and agreed to the published version of the manuscript.

Funding: The financial support from the Natural Science Foundation of Hunan Province for Distinguished Young Scholars (Grant No. 2021JJ10062) and the Guangdong Province Key-Area Research and Development Program of China (Grant No. 2019B010943001) is acknowledged by L. Zhang. Author, J. Guo, would like to thank the financial support by the National Science and Technology Major Project (2017-VI-0009-0080), Key-Area Research and Development Program of Guangdong Province (2019B010935001), as well as Industry and Information Technology Bureau of Shenzhen Municipality (Project No. 201806071354163490).

Data Availability Statement: The data presented in this study are available on request from the corresponding author.

Conflicts of Interest: The authors declare no conflict of interest.

References

1. Backman, D.G.; Williams, J.C. Advanced materials for aircraft engine applications. *Science* **1992**, *255*, 1082–1087. [CrossRef] [PubMed]
2. Joyce, M.R.; Wu, X.; Reed, P.A.S. The effect of environment and orientation on fatigue crack growth behaviour of CMSX-4 nickel base single crystal at 650 °C. *Mater. Lett.* **2004**, *58*, 99–103. [CrossRef]
3. Xiao, B.; Luan, J.; Zhao, S.; Zhang, L.; Chen, S.; Zhao, Y.; Xu, L.; Liu, C.T.; Kai, J.J.; Yang, T. Achieving thermally stable nanoparticles in chemically complex alloys via controllable sluggish lattice diffusion. *Nat. Commun.* **2022**, *13*, 4870. [CrossRef] [PubMed]
4. Wu, Y.; Li, C.; Xia, X.; Liang, H.; Qi, Q.; Liu, Y. Precipitate coarsening and its effects on the hot deformation behavior of the recently developed γ′-strengthened superalloys. *J. Mater. Sci. Technol.* **2021**, *67*, 95–104. [CrossRef]
5. Li, Q.; Chen, S.; Zhang, Y.; Deng, C.; Zhang, L. Stress-induced formation of μ-TCP phase during the early-stage interdiffusion process in the NiCrAlY/NiAlCoCrW model coating/superalloy system at ambient temperature. *J. Alloys Compd.* **2022**, *891*, 161980. [CrossRef]
6. Sreenu, B.; Sarkar, R.; Kumar, S.S.S.; Chatterjee, S.; Rao, G.A. Microstructure and mechanical behaviour of an advanced powder metallurgy nickel base superalloy processed through hot isostatic pressing route for aerospace applications. *Mater. Sci. Eng. A* **2020**, *797*, 140254. [CrossRef]
7. Chao, P.Z.; Wen, Z.J.; Yu, W.; Lei, Z.; Yue, T. Effects of solution temperatures on creep resistance in a powder metallurgy nickel-based superalloy. *Mater. Today Commun.* **2021**, *28*, 102573. [CrossRef]
8. Li, C.; Teng, J.; Yang, B.; Ye, X.; Liu, J.; Li, Y. Correlation between microstructure and mechanical properties of novel Co-Ni-based powder metallurgy superalloy. *Mater. Charact.* **2021**, *181*, 111480. [CrossRef]
9. Dudova, N.; Belyakov, A.; Sakai, T.; Kaibyshev, R. Dynamic recrystallization mechanisms operating in a Ni-20%Cr alloy under hot-to-warm working. *Acta Mater.* **2010**, *58*, 3624–3632. [CrossRef]
10. Yang, L.; Ren, X.; Ge, C.; Yan, Q. Status and development of powder metallurgy nickel-based disk superalloys. *Int. J. Mater. Res.* **2019**, *110*, 901–910. [CrossRef]
11. Baccino, R.; Moret, F.; Pellerin, F.; Guichard, D.; Raisson, G. High performance and high complexity net shape parts for gas turbines: The ISOPREC®powder metallurgy process. *Mater. Des.* **2000**, *21*, 345–350. [CrossRef]
12. Benjamin, J.S.; Larson, J.M. Powder metallurgy techniques applied to superalloys. *J. Aircr.* **1977**, *14*, 613–623. [CrossRef]
13. Wu, H.; Zhuang, X.; Nie, Y.; Li, Y.; Jiang, L. Effect of heat treatment on mechanical property and microstructure of a powder metallurgy nickel-based superalloy. *Mater. Sci. Eng. A* **2019**, *754*, 29–37. [CrossRef]
14. Hu, D.; Wang, T.; Ma, Q.; Liu, X.; Shang, L.; Li, D.; Pan, J.; Wang, R. Effect of inclusions on low cycle fatigue lifetime in a powder metallurgy nickel-based superalloy FGH96. *Int. J. Fatigue* **2019**, *118*, 237–248. [CrossRef]
15. Kuo, Y.; Kakehi, K. Effect of the prior particle boundary on the microstructure and mechanical properties of hot-isostatic-pressed IN718 alloy. *Mater. Trans.* **2017**, *58*, 1042–1048. [CrossRef]
16. Yang, Q.; Yang, X.; Huang, W.; Shi, Y.; Shi, D. Small fatigue crack propagation rate and behaviours in a powder metallurgy superalloy: Role of stress ratio and local microstructure. *Int. J. Fatigue* **2022**, *160*, 106861. [CrossRef]
17. Qu, J.L.; Zhang, X.; Yang, S.; Gu, Y.; Tao, Y. Research on inclusions in powder metallurgy superalloy—A review. *Powder Metall. Ind.* **2020**, *30*, 1–11. [CrossRef]
18. Ma, W.B.; Liu, G.Q.; Hu, B.F.; Jia, C.C. Formation of previous particle boundary of nickel base PM superalloy FGH96. *Acta Metall. Sin.* **2013**, *49*, 1248–1254. [CrossRef]
19. Qin, S.; Yan, L.; Zhang, X. Removing prior particle boundaries in a powder superalloy based on the interaction between pulsed electric current and chain-like structure. *J. Mater. Sci. Technol.* **2021**, *87*, 95–100. [CrossRef]
20. Hou, J.; Dong, J.X.; Yao, Z.H.; Jiang, H.; Zhang, M.C. Influences of PPB, PPB affect zone, grain boundary and phase boundary on crack propagation path for a P/M superalloy FGH4096. *Mater. Sci. Eng. A* **2018**, *724*, 17–28. [CrossRef]
21. Rao, G.A.; Srinivas, M.; Sarma, D.S. Influence of modified processing on structure and properties of hot isostatically pressed superalloy Inconel 718. *Mater. Sci. Eng. A* **2006**, *418*, 282–291. [CrossRef]
22. Chang, L.; Jin, H. A mechanistic study for the fracture mode and ductility variation in a powder metallurgy superalloy hot-isostatic-pressed at sub- and super-solvus temperatures. *Mater. Sci. Eng. A* **2019**, *743*, 733–740. [CrossRef]
23. Wallace, W.; Wiebe, W.; Whelan, E.; Dainty, R.; Terada, T. The effect of grain-boundary structure on the tensile fracture behaviour of hot-isostatically pressed 713LC alloy compacts. *Powder Metall.* **1973**, *16*, 416–436. [CrossRef]
24. Zhang, C.J.; Wang, P.; Wen, Z.X.; Xu, Z.Z.; He, P.F.; Yue, Z.F. Study on creep properties of nickel-based superalloy blades based on microstructure characteristics. *J. Alloys Compd.* **2022**, *890*, 161710. [CrossRef]
25. Qiu, C.L.; Attallah, M.M.; Wu, X.H.; Andrews, P. Influence of hot isostatic pressing temperature on microstructure and tensile properties of a nickel-based superalloy powder. *Mater. Sci. Eng. A* **2013**, *564*, 176–185. [CrossRef]
26. Teng, Q.; Xie, Y.; Sun, S.; Xue, P.; Long, A.; Wu, T.; Cai, C.; Guo, J.; Wei, Q. Understanding on processing temperature-metallographic microstructure-tensile property relationships of third-generation nickel-based superalloy WZ-A3 prepared by hot isostatic pressing. *J. Alloys Compd.* **2022**, *909*, 164668. [CrossRef]
27. Ma, W.; Liu, G.; Hu, B.; Zhang, Y.; Liu, J. Effect of Hf on carbides of FGH4096 superalloy produced by hot isostatic pressing. *Mater. Sci. Eng. A* **2013**, *587*, 313–319. [CrossRef]
28. Zhao, J.P.; Yu, T.; Yuan, S.Q.; Jia, J.; Han, S.B. The problem of prior particle boundary precipitation in P/M superalloys. *Powder Metall. Ind.* **2010**, *20*, 43–49. [CrossRef]

29. Chang, L.; Sun, W.; Cui, Y.; Yang, R. Preparation of hot-isostatic-pressed powder metallurgy superalloy Inconel 718 free of prior particle boundaries. *Mater. Sci. Eng. A* **2017**, *682*, 341–344. [CrossRef]
30. Rao, G.A.; Srinivas, M.; Sarma, D.S. Effect of solution treatment temperature on microstructure and mechanical properties of hot isostatically pressed superalloy Inconel*718. *Mater. Sci. Technol.* **2004**, *20*, 1161–1170. [CrossRef]
31. Tan, L.; Li, Y.; Liu, F.; Nie, Y.; Jiang, L. Microstructure evolutions of a powder metallurgy superalloy during high-strain-rate deformation. *J. Alloys Compd.* **2019**, *789*, 506–517. [CrossRef]
32. Higashi, M.; Kanno, N. Evaluation of hot workability of powder metallurgy Ni-based superalloy with different initial microstructures. *Metall. Mater. Trans.* **2021**, *52*, 181–193. [CrossRef]
33. Tan, L.M.; Li, Y.P.; Liu, C.Z.; Yang, C.; Ding, H.H.; Huang, L.; Liu, F.; Qin, Z.J.; Jiang, L. The evolution history of superalloy powders during hot consolidation and powders plastic deformation. *Mater. Charact.* **2018**, *140*, 30–38. [CrossRef]
34. Darling, K.A.; Kapoor, M.; Kotan, H.; Hornbuckle, B.C.; Walck, S.D.; Thompson, G.B.; Tschopp, M.A.; Kecskes, L.J. Structure and mechanical properties of Fe–Ni–Zr oxide-dispersion-strengthened (ODS) alloys. *J. Nucl. Mater.* **2015**, *467*, 205–213. [CrossRef]
35. Barton, D.J.; Kale, C.; Hornbuckle, B.C.; Darling, K.A.; Solanki, K.N.; Thompson, G.B. Microstructure and dynamic strain aging behavior in oxide dispersion strengthened 91Fe-8Ni-1Zr (at%) alloy. *Mater. Sci. Eng. A* **2018**, *725*, 503–509. [CrossRef]
36. Kotan, H.; Darling, K.A.; Luckenbaugh, T. High Temperature Mechanical Properties and Microstructures of Thermally Stabilized Fe-Based Alloys Synthesized by Mechanical Alloying Followed by Hot Extrusion. *Met. Mater. Int.* **2021**, *27*, 1790–1797. [CrossRef]
37. Song, K.; Aindow, M. Grain growth and particle pinning in a model Ni-based superalloy. *Mater. Sci. Eng. A* **2008**, *479*, 365–372. [CrossRef]
38. Central South University, Shenzhen Wedge Central South Research Institute Co., Ltd. A Nickel Base Superalloy and Its Preparation Methods. China Patent CN106282667A, 4 January 2017. Available online: https://d.wanfangdata.com.cn/patent/ChJQYXRlbnROZXdTMjAyMTAxMDkSEENOMjAxNTEwMzIyOTMyLjIaCDl4YmZ5aGRt (accessed on 4 January 2017).
39. Liu, L.R.; Jin, T.; Zhao, N.R.; Sun, X.F.; Guan, H.R.; Hu, Z.Q. Formation of carbides and their effects on stress rupture of a Ni-base single crystal superalloy. *Mater. Sci. Eng. A* **2003**, *361*, 191–197. [CrossRef]
40. Matysiak, H.; Zagorska, M.; Andersson, J.; Balkowiec, A.; Cygan, R.; Rasinski, M.; Pisarek, M.; Andrzejczuk, M.; Kubiak, K.; Kurzydlowski, K.J. Microstructure of Haynes((R)) 282((R)) Superalloy after Vacuum Induction Melting and Investment Casting of Thin-Walled Components. *Materials* **2013**, *6*, 5016–5037. [CrossRef]
41. Li, F.; Fu, R.; Yin, F.; Feng, D.; Wang, H.; Du, G.; Feng, Y. Impact of γ'(Ni_3(Al,Ti)) phase on dynamic recrystallization of a Ni-based disk superalloy during isothermal compression. *J. Alloys Compd.* **2017**, *693*, 1076–1082. [CrossRef]
42. Yang, J.; Luo, J.; Li, X.; Li, M. Evolution mechanisms of recrystallized grains and twins during isothermal compression and subsequent solution treatment of GH4586 superalloy. *J. Alloys Compd.* **2021**, *850*, 156732. [CrossRef]
43. Zhou, X.; Ma, T.F.; Li, Y.L.; Li, L.; Wang, K.X.; Zhang, Y.S.; Lai, Y.J.; Zhang, P.X. Secondary γ' evolution and relationship to hot deformation behavior of a supersolvus-treated superalloy with high precipitate volume fraction. *Mater. Sci. Eng. A* **2019**, *761*, 138046. [CrossRef]
44. Rui, S.-S.; Han, Q.-N.; Wang, X.; Li, S.; Ma, X.; Su, Y.; Cai, Z.; Du, D.; Shi, H.-J. Correlations between two EBSD-based metrics Kernel Average Misorientation and Image Quality on indicating dislocations of near-failure low alloy steels induced by tensile and cyclic deformations. *Mater. Today Commun.* **2021**, *27*, 102445. [CrossRef]
45. Tian, S.; Xie, J.; Zhou, X.; Qian, B.; Lun, J.; Yu, L.; Wang, W. Microstructure and creep behavior of FGH95 nickel-base superalloy. *Mater. Sci. Eng. A* **2011**, *528*, 2076–2084. [CrossRef]
46. He, L.Z.; Zheng, Q.; Sun, X.F.; Guan, H.R.; Hu, Z.Q.; Tieu, A.K.; Lu, C.; Zhu, H.T. Effect of carbides on the creep properties of a Ni-base superalloy M963. *Mater. Sci. Eng. A* **2005**, *397*, 297–304. [CrossRef]

Disclaimer/Publisher's Note: The statements, opinions and data contained in all publications are solely those of the individual author(s) and contributor(s) and not of MDPI and/or the editor(s). MDPI and/or the editor(s) disclaim responsibility for any injury to people or property resulting from any ideas, methods, instructions or products referred to in the content.